Supplementary information for "The influence of ground shaking on the distribution and size of coseismic landslides from the M_w 7.6 2005 Kashmir earthquake"

Audrey M. Dunham[1,2*], Eric Kiser[1], Jeffrey S. Kargel[3], Umesh K. Haritashya[4], C. Scott Watson[5], Dan H. Shugar[6]

[1]*Department of Geoscience, University of Arizona, Tucson, AZ, 85721*
[2]*US Geological Survey, Seattle Field Office, Seattle WA, 98195*
[3]*Planetary Science Institute, Tucson AZ, 85719*
[4]*Department of Geology and Environmental Geosciences, University of Dayton, Dayton, OH 45469*
[5]*COMET, School of Earth and Environment, University of Leeds, Leeds, LS2 9JT, UK*
[6]*Water, Sediment, Hazards, and Earth-surface Dynamics (waterSHED) Lab, Department of Geoscience, University of Calgary, Canada*
**Corresponding author: adunham@usgs.gov*

Contents:

Supplementary Text:

Text S1: *Model validation*

Text S2: *Calculation of landslide location along hillslope*

Text S3: *Calculation of landslide frequency area distribution (FAD)*

Supplementary Figures:

Figure S1: *Slip and rise time of 5 source time functions for individual subfaults.*

Figure S2: *PGV and amplification maps for simulations using a homogeneous velocity model*

Figure S3: *Model validation comparing GMMs to synthetic PGV.*

Figure S4: *Comparison of flat mesh elevations for amplification calculation.*

Figure S5: *Rpcrest with different "microcell" sizes.*

Figure S6: *Snapshots of the peak horizontal velocity wavefield.*

Supplementary Movie Captions:

Supplementary movies can be found at 10.5281/zenodo.12534705

Movie S1: Movie of the vertical velocity wavefield from the low frequency source ORIG through time where red and blue are positive and negative velocity (positive = Up, negative = Down). Black star shows the location of the epicenter of the earthquake and the black line with red triangles shows the surface rupture.

Movie S2: Movie of the absolute value of the maximum horizontal velocity wavefield from the low frequency source ORIG through time. Black star shows the location of the epicenter of the earthquake and the black line with red triangles shows the surface rupture.

Movie S3: Movie of the vertical velocity wavefield from the high frequency source HF through time where red and blue are positive and negative velocity (positive = Up, negative = Down). Black star shows the location of the epicenter of the earthquake and the black line with red triangles shows the surface rupture.

Movie S4: Movie of the absolute value of the maximum horizontal velocity wavefield from the high frequency source HF through time. Black star shows the location of the epicenter of the earthquake and the black line with red triangles shows the surface rupture.

Supplementary Text

Text S1: *Model validation*

There are no available seismometers or high-rate GPS stations in the modeled region from this earthquake to compare to our ground shaking data. To validate synthetic ground motions, we compare our simulations to the USGS ShakeMap. This uses the NGA-West2 database attenuation relationships (Abrahamson et al., 2014; Boore et al., 2014; Campbell & Bozorgnia, 2014; Chiou & Youngs, 2014) and felt intensity data to calculate PGV with a uniform V_{s30} = 760 m/s. Because there were no near-field stations to record ground shaking, only reported intensity values are included in the ShakeMap, likely leading to large uncertainties. Fig. S3 shows the comparison of ShakeMap to the simulations for both ORIG (low frequency) and HF (high frequency) using a homogeneous velocity model (dashed lines) and a 1D velocity model with a 1 km slower velocity layer with a linear gradient to 1500 m/s at the surface (solid lines). We also plot the felt intensity values used in the USGS ShakeMap as gray circles. Both ORIG and HF for the homogeneous model have much lower PGVs, therefore we discount them in further analysis. For the simulations with a slower velocity layer at the surface, ORIG clearly has much lower PGV values compared to ShakeMap while HF has lower PGV values but is more comparable overall, leading us to conclude that ORIG is less realistic compared to HF. We expect that the HF simulations will be somewhat different compared to ShakeMap because (1) our simulations are not capturing the entire range of frequencies that likely influence the highest felt intensities near the fault, (2) ShakeMap uses a lower V_{s30} value, and (3) GMMs with uniform site conditions typically produce homogeneous ground motions along the length of the fault (Rrup = 0 km) whereas our simulations have variable slip and rupture dynamics along the fault that is being averaged and likely decreasing the near-fault average values, illustrated by the increase in the spread of values in Fig. S2 for ORIG and HF compared to ShakeMap.

Fig. S3c shows the comparison of the points along the fault used in the averaged lines in (a) and (b) for PGV from HF in a layered model and ShakeMap. This shows that HF primarily has weaker ground motions compared to the ShakeMap except for where we see a peak up to ~140 cm/s located at the surface rupture due to directivity and the rupturing of the main slip asperity. This also shows that points on the footwall have higher PGVs compared to the ShakeMap. This mismatch on the footwall is likely due to the higher ground shaking that we see in our simulations in the southwest due to directivity of the wavefield causing unexpectedly high amplitudes across the fault. Overall, there is considerable overlap between PGV values from the HF simulation with the low velocity layer and ShakeMap. This is not a perfect match and without a detailed 3D velocity model of the region, specifically including details of near-surface velocities, or recorded waveforms to use for validation, these simulation results should not be used for primary seismic hazard analysis.

Text S2: *Calculation of landslide location along hillslope*

The locations of landslides along the hillslope can be indicative of particular mechanisms and triggers, with previous studies showing that earthquake triggered landslides tend to cluster closer to ridges than rainfall triggered landslides (Meunier et al., 2007; Rault et al., 2019). To calculate the location of the landslides along the hillslope, we employ the method of Rault et al., (2019). First, we calculate the normalized distance to the river which is defined as:

$$| d_{st} | = \frac{d_{st}}{d_{st} + d_{tp}} \qquad \text{(Eq. 1)}$$

Where d_{st} and d_{tp} are the minimum distance to a river and ridge, respectively. This value is normalized to the hillslope length on which the landslide is located. This equation gives us a value between 0 and 1, where 0 is located at the river and 1 is located at the ridge. $|d_{st}|$ is highly dependent on how the locations of ridges and rivers are mapped, which are defined using the methods outlined in the supplement of Dunham et al. (2022) and a river extraction threshold of 10^7 m^2 of contributing upslope area. We calculate the probability density functions (PDF) of d_{st} for just the cells (from 30 m resolution DEM) effected by landslides (PDF_{ls}) and all of the cells in the study region (PDF_{topo}) and define the ratio of probability R_p as:

$$R_p = \frac{PDF_{ls}}{PDF_{topo}} \qquad \text{(Eq. 2)}$$

Rp normalizes the location along the hillslope to the topography, removing any bias that was introduced due to the method of mapping rivers and ridges. Rp is calculated for "macrocells" that are 4.5 km x 4.5 km, 6 km x 6 km, and 10 km x 10 km to show how the value changes with varying "macrocell" sizes (Fig. S5). Amongst these, only "macrocells" of 4.5 km x 4.5 km show significant spatial variations and therefore are used to inform our interpretations of the landslide catalog. For the PDF_{ls}, we use a minimum threshold of 30 cells containing landslides within each larger "macrocell", otherwise that "macrocell" is removed. $Rp >> 1$ for values of $|d_{st}| >0.75$, and $Rp >> 1$ for values of $|d_{st}| < 0.25$ define crest and toe clustering, respectively. Rp_{crest} is the average Rp within a "macrocell" of values of $|d_{st}| >0.75$ and Rp_{toe} is the average Rp within a "macrocell" of values of $|d_{st}| < 0.25$. Because Rp_{crest} and Rp_{toe} are mutually exclusive, we report only Rp_{crest} values.

Text S3*:* *Calculation of landslide frequency area distribution (FAD)*

Landslide catalogs exhibit a distinct power-law relationship between area and frequency for larger landslides and a roll-over for smaller landslides. Frequency-area distributions (FAD) can be characterized by fitting the power-law with a power-law exponent, α, to demonstrate the relative distribution of large and small landslides for various subsets of the landslide catalog. A distribution with a higher frequency of large landslides is fit with a smaller (less negative) value of α, where a lower frequency of large landslides is fit with a larger (more negative) value of α We determine FADs and values of α using the methods of Clauset et al. (2009) for various subsets of the landslide database including positive and negative amplification, high and low values of PGV, steep and gentle slopes, high and low elevations, and within and outside of the Muzaffarabad Fm to investigate how these parameters influence landslide size. α is calculated:

$$\alpha = 1 + n\left[\sum_{i=1}^{n} ln(\frac{x_i}{x_{min}})\right]^{-1} \qquad \text{(Eq. 3)}$$

Where x_i, i=1,2,…n are observed values of x (the distribution of landslide areas) such that x_i is greater than x_{min}, i.e. where the curve shows a deflection away from the power-law. For this data set, we set x_{min} to 17^3 m^2. We calculate error for α using the standard error estimate in the maximum likelihood estimation, $\sigma = (\alpha - 1)/\sqrt{n}$.

Supplementary Figures

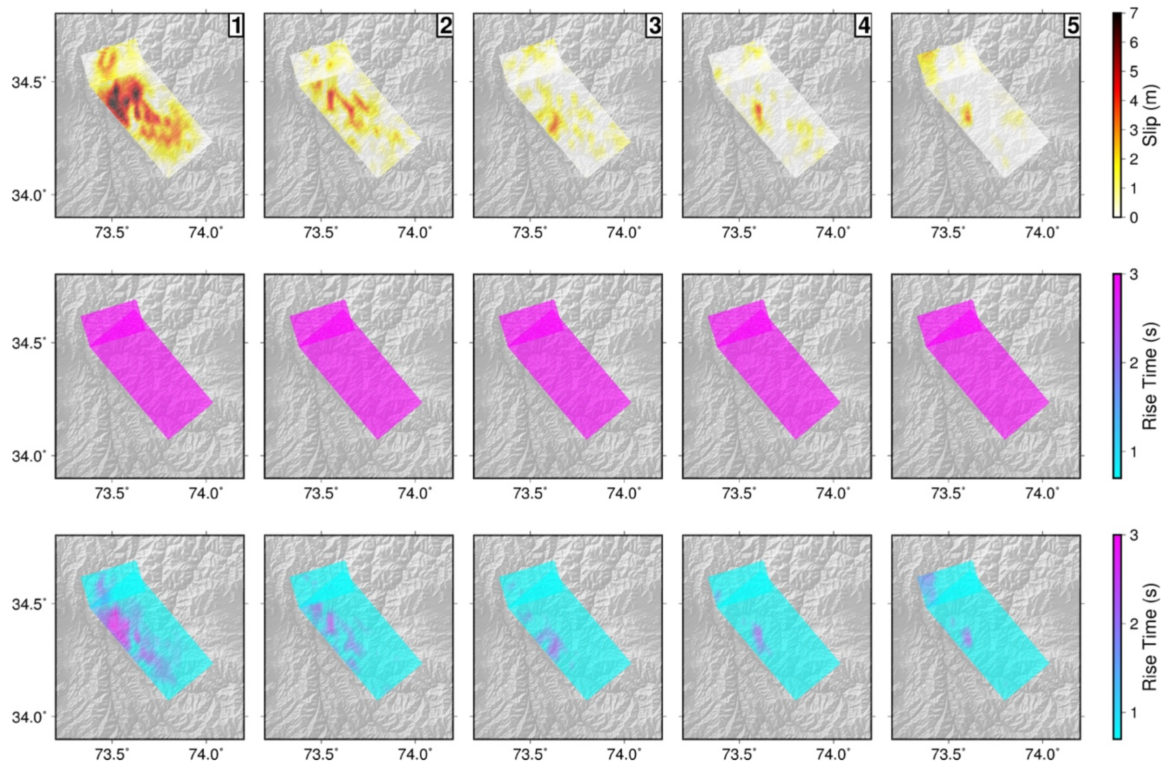

Figure S1: ***Slip and rise time of 5 source time functions for individual subfaults.*** **(top)** slip model from Avouac et al. (2006). Each source has 5 source time functions which are shown here as numbers 1 through 5. In the original model, each subfault has a rise time of 3s and 1-5 source time functions start 1.5s (50%) after the previous source time function. **(middle)** constant rise times from ORIG **(bottom)** modified rise times based on Eq. 1 from the main text, defining the rise time distribution of HF.

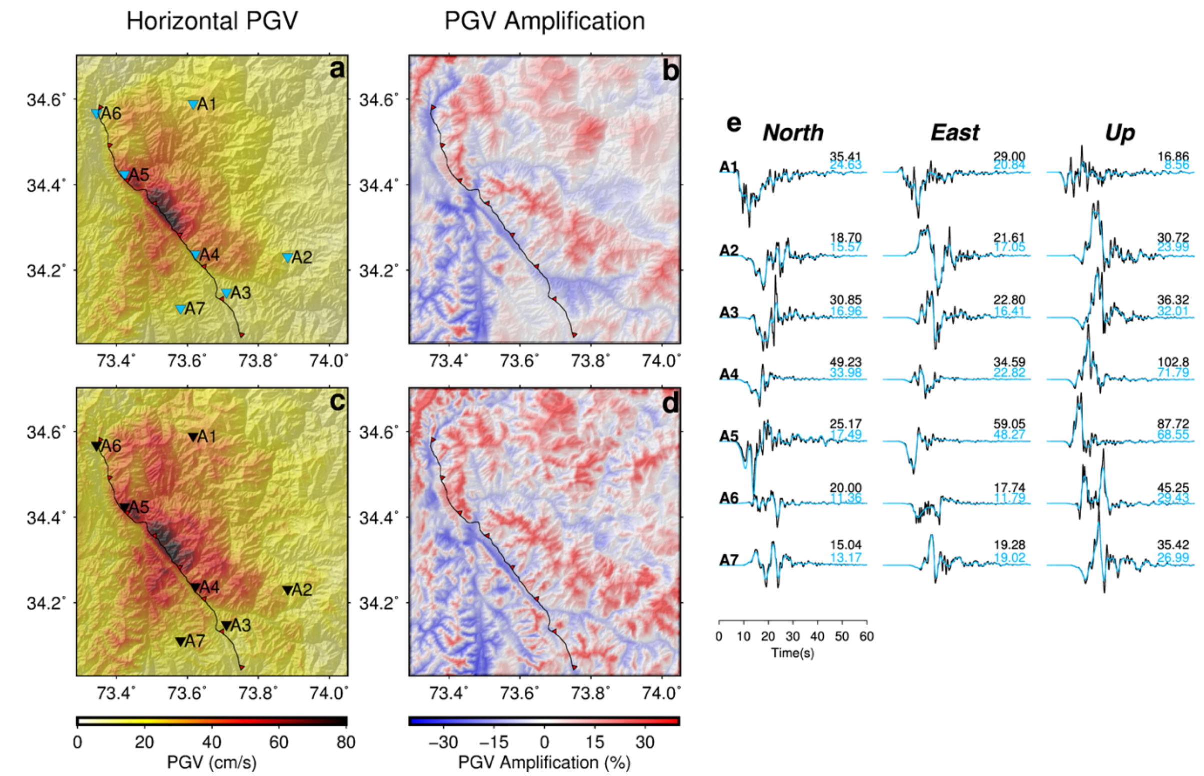

Figure S2: ***PGV and amplification maps for simulations using a homogeneous velocity model.*** **(a)** Horizontal PGV and **(b)** amplification for ORIG. **(c)** Horizontal PGV and **(d)** amplification for HF. Line denotes surface rupture. **(e)** Example waveforms for the north, east, and vertical component of 7 stations (plotted on a/c) for ORIG (blue triangles) and HF (black triangles). PGV of each seismogram labeled in cm/s (ORIG – blue, HF – black).

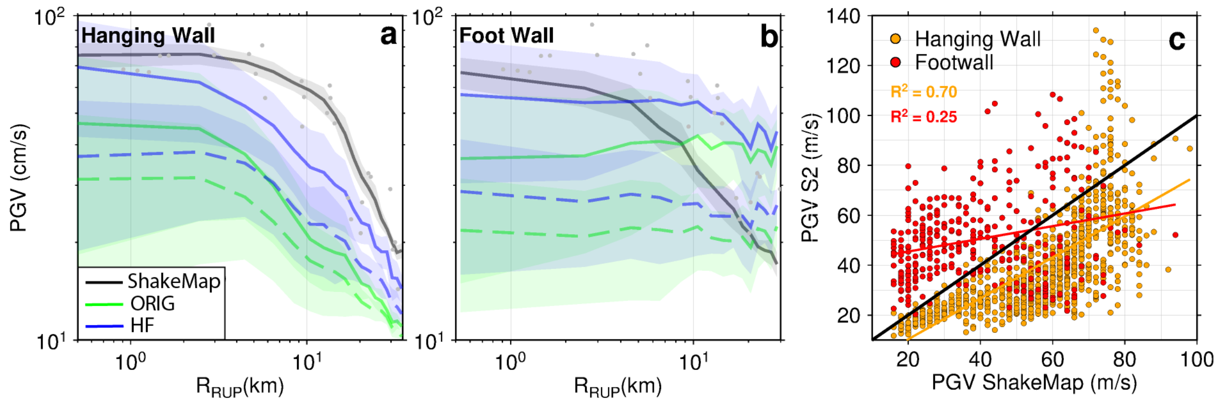

Figure S3: ***Model validation comparing USGS ShakeMap to synthetic PGV.*** **(a)** Hanging wall and **(b)** footwall measurements of PGV related to the distance from the fault surface (R_{Rup}). Solid black lines are PGVs from the USGS ShakeMap and accompanying felt intensities (gray circles). Green and blue lines are PGV from ORIG and HF synthetic sources, respectively. Dashed and solid lines denote homogeneous and layered velocity models, respectively. **(c)** ShakeMap PGV vs HF PGV with the layered velocity model. Circles are colored by hanging wall (orange) or footwall (red) and black solid line shows a 1-1 ratio. Orange and red lines represent the best fit lines to the hanging and footwall, respectively, with R^2 values denoted in their corresponding color.

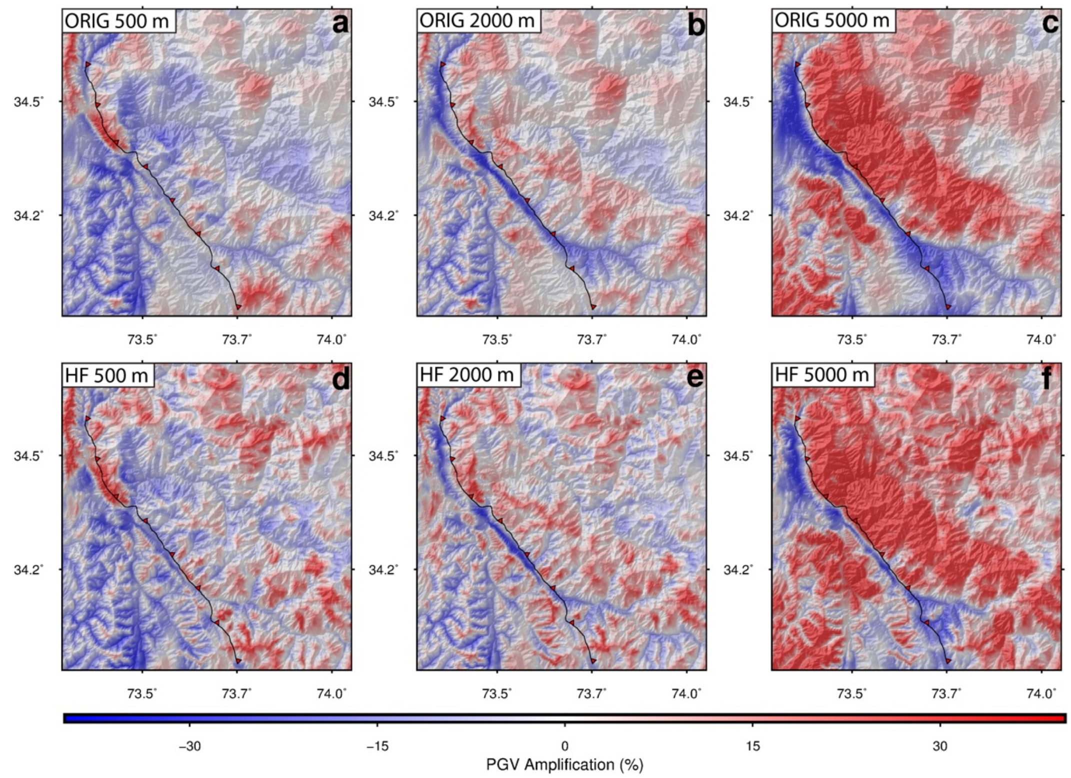

Figure S4: ***Comparison of flat mesh elevations for amplification calculation.*** **(a-c)** PGV amplification calculated for ORIG with a homogeneous velocity model using progressively higher elevation flat meshes, elevations labeled. **(d-f)** PGV amplification calculated for HF using progressively higher elevation flat meshes, elevations labeled. We choose these elevations as the minimum, average, and maximum elevations of the topography within our study region.

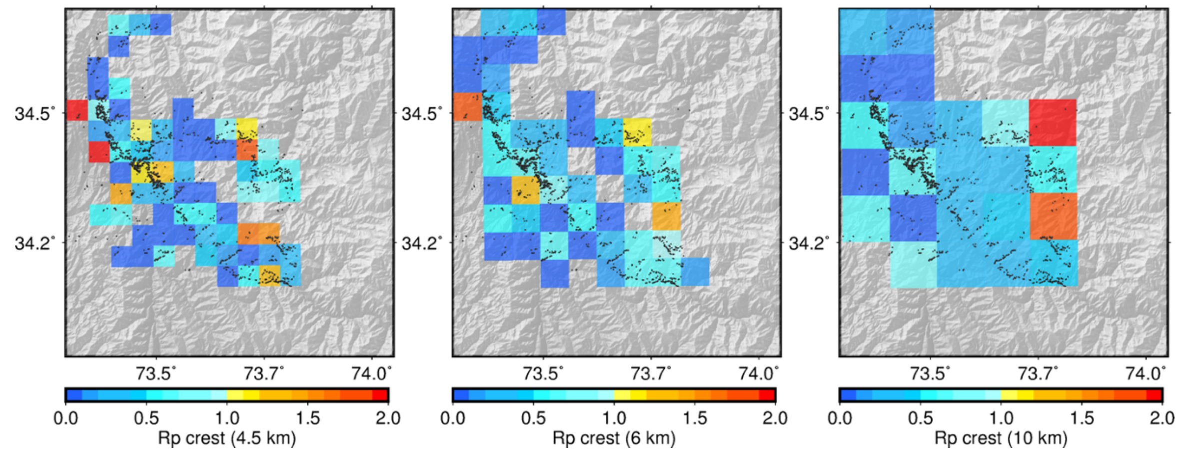

Figure S5: ***Rpcrest with different "microcell" sizes.*** Calculated Rp_{crest} values for macrocells with varying sizes; **(left)** 4.5 x 4.5 km **(middle)** 6 km x 6 km **(right)** 10 km x 10 km. Warm colors indicate crest clustering and cool colors indicate toe clustering.

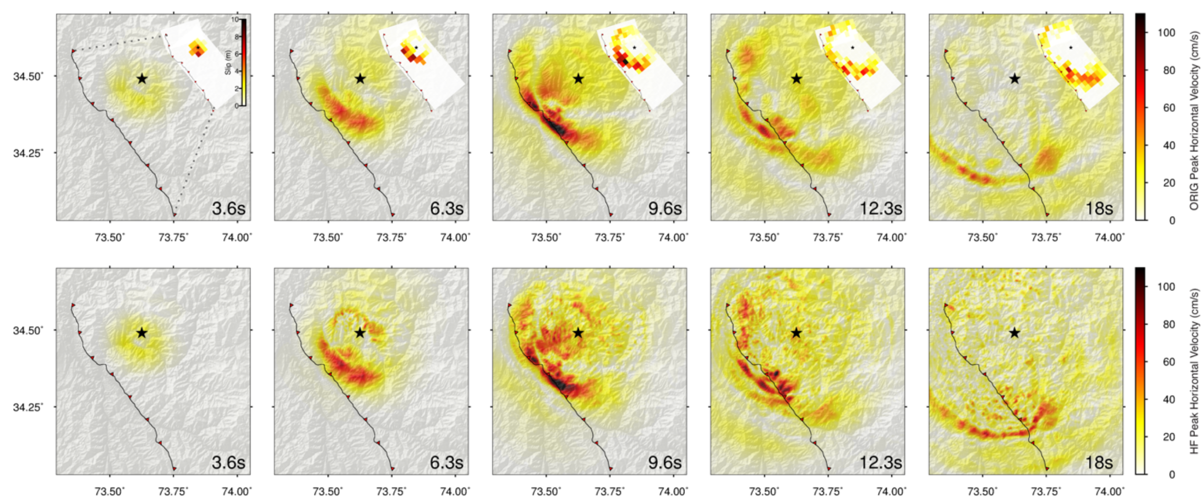

Figure S6: ***Snapshots of the peak horizontal velocity wavefield.*** **(top)** Source ORIG. **(bottom)** Source HF. Black star is the epicenter, line with red triangles denotes the surface rupture, and timestamps are shown in the lower right corner for each snapshot. Inset shows the slip on the fault at each time step as the sum of slip between each snapshot.

References

Abrahamson, N. A., Silva, W., & Kamai, R. (2014). Summary of the ASK14 Ground Motion Relation for Active Crustal Regions. *Earthquake Spectra*, *30*(3), 1025–1055. https://doi.org/10.1193/070913EQS198M

Avouac, J. P., Ayoub, F., Leprince, S., Konca, O., & Helmberger, D. V. (2006). The 2005, Mw 7.6 Kashmir earthquake: Sub-pixel correlation of ASTER images and seismic waveforms analysis. *Earth and Planetary Science Letters*, *249*, 514–528. https://doi.org/10.1016/j.epsl.2006.06.025

Boore, D. M., Stewart, J. P., Seyhan, E., & Atkinson, G. M. (2014). NGA-West2 Equations for Predicting PGA, PGV, and 5% Damped PSA for Shallow Crustal Earthquakes: *Earthquake Spectra*, *30*(3), 1057–1085. https://doi.org/10.1193/070113EQS184M

Campbell, K. W., & Bozorgnia, Y. (2014). NGA-West2 Ground Motion Model for the Average Horizontal Components of PGA, PGV, and 5% Damped Linear Acceleration Response Spectra. *Earthquake Spectra*, *30*(3), 1087–1114. https://doi.org/10.1193/062913EQS175M

Chiou, B. S. J., & Youngs, R. R. (2014). Update of the Chiou and Youngs NGA Model for the Average Horizontal Component of Peak Ground Motion and Response Spectra. *Earthquake Spectra*, *30*(3), 1117–1153. https://doi.org/10.1193/072813EQS219M

Clauset, A., Shalizi, C. R., & Newman, M. E. J. (2009). Power-law distributions in empirical data. In *Society for Industrial and Applied Mathematics* (Vol. 51, Issue 4, pp. 661–703). https://doi.org/10.1137/070710111

Dunham, A. M., Kiser, E., Kargel, J. S., Haritashya, U. K., Watson, C. S., Shugar, D. H., Hughes, A., & DeCelles, P. G. (2022). Topographic Control on Ground Motions and Landslides From the 2015 Gorkha Earthquake. *Geophysical Research Letters*, *49*(10), e2022GL098582. https://doi.org/10.1029/2022GL098582

Meunier, P., Hovius, N., & Haines, A. J. (2007). Regional patterns of earthquake-triggered landslides and their relation to ground motion. *Geophysical Research Letters*, *34*(20). https://doi.org/10.1029/2007GL031337

Rault, C., Robert, A., Marc, O., Hovius, N., & Meunier, P. (2019). Seismic and geologic controls on spatial clustering of landslides in three large earthquakes. *Earth Surface Dynamics*, *7*, 829–839. https://doi.org/10.5194/esurf-7-829-2019